as a supernova or a thermally pulsing asymptotic giant branch star or a Wolf-Rayet star) and the formation of some of the early solar system objects in which their records are found by considering stellar nucleosynthesis yields and a suitable model for transport into and subsequent mixing of the radioactivities with the protosolar cloud [e.g. (1)]. If a homogeneous distribution of the short-lived nuclides in the solar nebula is assumed, they may be used as relative chronometers for dating solar system events and processes.
11. S. Yoneda, L. Grossman, *Geochim. Cosmochim. Acta* **59**, 823 (1995).
12. S. Sahijpal, J. N. Goswami, A. M. Davis, *Geochim. Cosmochim. Acta* **64**, 1989 (2000).
13. T. R. Ireland, *Geochim. Cosmochim. Acta* **54**, 3219 (1990).
14. The symbol δ is used to represent the magnitude of abundance anomaly in a given isotope with respect to a reference isotope. In the case of ^{48}Ca and ^{50}Ti, the reference isotopes are ^{44}Ca and ^{48}Ti, respectively. In general, the abundance anomaly in a given isotope can be expressed as $\delta^iM = \{[(^iM/^jM)_{sample}/(^iM/^jM)_{standard}] - 1\} \times 1000‰$, where *j* represents the reference isotope. A suitable standard with normal isotopic composition is used to infer the magnitude of the anomaly.
15. S. Sahijpal, J. N. Goswami, A. M. Davis, L. Grossman, R. S. Lewis, *Nature* **391**, 559 (1998).
16. G. J. MacPherson, A. M. Davis, E. K. Zinner, *Meteoritics* **30**, 365 (1995).
17. G. Srinivasan, S. Sahijpal, A. A. Ulyanov, J. N. Goswami, *Geochim. Cosmochim. Acta* **60**, 1823 (1996).
18. Samples were analyzed with a Cameca ims-4f ion microprobe at the Physical Research Laboratory, Ahmedabad. Techniques are described in supplemental data on *Science* Online.
19. The correlation between the excess in the daughter nuclide abundance and the abundance of a stable nuclide of the parent element (^{10}B and ^{9}Be in the present case), relative to a suitable normalizing isotope (^{11}B), suggests that the excess is due to in situ decay of the parent nuclide (^{10}Be). The measured isotopic abundance ratio of the boron isotopes can be expressed as $(^{10}B/^{11}B)_m = (^{10}B/^{11}B)_i + [(^{10}Be/^{9}Be)_i \times (^{9}Be/^{11}B)_m]$, where the subscripts m and i denote measured and initial, respectively. In obtaining the value of $(^{10}Be/^{9}Be)_i$ in the analyzed hibonite, we have not corrected for the amount of stable ^{9}Be produced along with radioactive ^{10}Be during energetic particle irradiation of nebular material. This is justified because of the production ratio of ~0.1 for ^{10}Be/^{9}Be, which can account for only a few percent of ^{9}Be measured in the hibonite; furthermore, the correction would be much smaller than the uncertainties introduced by the errors in the measured ^{9}Be/^{11}B and ^{10}B/^{11}B ratios (Table 1). We used the Isochron program (37) to analyze the data. For obtaining initial $(^{10}Be/^{9}Be)_i$ for individual hibonite, we assume normal B composition ($^{10}B/^{11}B = 0.2473$) in them; no such assumption was made while analyzing the combined data set (Fig. 1).
20. J. N. Goswami, K. D. McKeegan, K. K. Marhas, N. Sinha, A. M. Davis, *Lunar Planet. Sci.* **XXXII**, 1576 (2001).
21. K. K. Marhas, thesis, Devi Ahilya University, Indore, India (2001).
22. A. Hashimoto, R. W. Hinton, A. M. Davis, L. Grossman, T. K. Mayeda, R. N. Clayton, *Lunar Planet. Sci.* **XVII**, 317 (1986).
23. If a time delay is introduced between the production of the short-lived nuclides and the formation of solids in the solar nebula into which they became incorporated, their abundances will be depleted because of free decay; the depletion factor will depend on the time delay and half-lives of the nuclides, with maximum depletion for the shortest lived nuclide. However, a decay interval cannot explain the differences between the initial ^{10}Be and ^{26}Al abundances in the hibonite (Table 1) and their canonical early solar system values ($^{10}Be/^{9}Be \sim 10^{-3}$ and $^{26}Al/^{27}Al = 5 \times 10^{-5}$).
24. A. G. W. Cameron, *Astrophys. J.* **562**, 456 (2001).
25. Low-energy particle irradiation of the protosolar cloud before or during its collapse, leading to production of isotopes of Li, Be, and B as well as several short-lived nuclides (^{41}Ca, ^{26}Al, ^{53}Mn), was considered as a distinct possibility (38) after the reported observation of enhanced flux of gamma rays from the Orion star-forming region that was suggestive of the presence of a high flux of low-energy particles in star-forming molecular cloud complexes. However, a later reanalysis of the same data set showed that the earlier observation and inferences were erroneous (26). One of the reviewers suggested that a linear increase in metallicity over the lifetime of our galaxy may bring down the required enhancement of GCR flux needed to account for the observed ^{10}Be, and therefore this possibility cannot be ruled out. However there is neither any rigorous published work nor any general consensus on this issue at present.
26. H. Bleomen *et al.*, *Astrophys. J.* **521**, L137 (1999).
27. We consider an active early Sun as the source of the SEPs and represent them using the conventional power law in *E*, $dN/dE \propto E^{-\gamma}$, and exponential in *R*, $dN/dR \propto \exp(-R/R_o)$. We use a set of values for the power-law exponent γ (2 to 5) and for the characteristic rigidity R_o (50 to 400 MV) that cover the range seen in contemporary solar flares. The integral flux of protons above 10 MeV amu^{-1} was normalized to a fixed value in each case. Both proton-induced and α particle–induced reactions were taken into account assuming an α-to-proton ratio of 0.1. We consider irradiation of nebular solids of CI chondritic composition representing precursors of early solar system objects such as hibonite grains and CAIs. The targets were assumed to be spherical, with sizes varying from 10 μm to 1 cm, and to be characterized by a power-law size distribution of the type $dn/dr \propto r^{-\beta}$ (where *n* is the number and *r* is the radius of the targets), with β values of 3 to 5. We ignore possible shielding of the targets by nebular gas and assume free access of SEPs up to the asteroidal zone. Appropriate reaction cross sections for relevant reactions have been used in these calculations (38, 39).
28. K. D. McKeegan *et al.*, *Lunar Planet. Sci.* **XXXII**, 2175 (2001).
29. G. J. MacPherson, G. R. Huss, A. M. Davis, *Geochim. Cosmochim. Acta*, in press.
30. N. Sugiura, Y. Shuzou, A. Ulyanov, *Meteorit. Planet. Sci.* **36**, 1397 (2001).
31. G. Srinivasan, *Meteorit. Planet. Sci.* **36**, A195 (2001).
32. The effective production of ^{10}Be needs high-energy (>50 MeV) protons, whereas ^{41}Ca and ^{26}Al are mainly produced by low-energy (<30 MeV) particles [see (39, 39)]. This difference makes SEP production of ^{10}Be, relative to ^{41}Ca and ^{26}Al, sensitively dependent on the spectral parameters. For a given flux normalization, production of ^{10}Be will increase as the energy spectrum becomes flatter [decreasing value of γ or increasing value of R_o (27)], whereas the reverse is the case for ^{41}Ca and ^{26}Al.
33. R. C. Reedy, *Proc. Indian Acad. Sci.* (*Earth Planet. Sci.*) **107**, 433 (1998).
34. M. W. Caffee, C. M. Hohenberg, T. D. Swindle, J. N. Goswami, *Astrophys. J.* **313**, L31 (1987).
35. Irradiation of different parcels of solar nebula material of varying composition by SEPs with different characteristics can lead to production of the three nuclides (^{26}Al, ^{41}Ca, and ^{10}Be) and provide source material from which CAIs from CV meteorites hosting these nuclides may have formed. However, it is not possible to match the initial solar system abundances of these nuclides unless ad hoc target compositions are considered [see, e.g., (8, 9, 29)]. Further, the observation of variable ^{10}Be/^{9}Be ratios in these CAIs with close to canonical ^{26}Al/^{27}Al ratios cannot be explained in this scenario.
36. S. Sahijpal, J. N. Goswami, *Astrophys. J.* **509**, L137 (1998).
37. A. Provost, *Chem. Geol.* **80**, 85 (1990).
38. R. Ramaty, B. Kozlovsky, R. E. Lingenfelter, *Astrophys. J.* **456**, 525 (1996).
39. J. N. Sisterson, K. Kim, M. W. Caffee, M. Imamura, R. C. Reedy, *Lunar Planet. Sci.* **XXVIII**, 1329 (1997).
40. We thank E. Olsen for sample SH-7, R. S. Lewis for the acid-resistant residue of Murchison, and M. Chaussidon for the GB4 standard (18). Supported by the Department of Space, India (K.K.M., J.N.G.) and by NASA grant NAG5-9510 (A.M.D.).

Supporting Online Material
www.sciencemag.org/cgi/content/full/298/5601/2182/DC1
Materials and Methods

10 September 2002; accepted 6 November 2002

A Late Triassic Impact Ejecta Layer in Southwestern Britain

Gordon Walkden,[1]* Julian Parker,[1] Simon Kelley[2]

Despite the 160 or so known terrestrial impact craters of Phanerozoic age, equivalent ejecta deposits within distal sedimentary successions are rare. We report a Triassic deposit in southwestern Britain that contains spherules and shocked quartz, characteristic of an impact ejecta layer. Inter- and intragranular potassium feldspar from the deposit yields an argon-argon age of 214 ± 2.5 million years old. This is within the age range of several known Triassic impact craters, the two closest of which, both in age and location, are Manicouagan in northeastern Canada and Rochechouart in central France. The ejecta deposit provides an important sedimentary record of an extraterrestrial impact in the Mesozoic that will help to decipher the number and effect of impact events, the source and dynamics of the event that left this distinctive sedimentary marker, and the relation of this ejecta layer to the timing of extinctions in the fossil record.

Major bolide impacts produce craters that may survive long after associated ejecta deposits have been lost through erosion or diagenetic alteration. There are five known late Triassic impact craters (*1*), including the 100-km-diameter Manicouagan crater (Fig. 1), which is one of the largest known Phanerozoic impacts (*2*). Earth experienced a series of worldwide extinctions in the late Triassic, constituting one of the top five Phanerozoic faunal crises (*3*, *4*), but the exact causes are disputed. The discovery of an ejecta deposit corresponding to one or more of these impact

[1]Department of Geology and Petroleum Geology, Kings College, University of Aberdeen, Aberdeen AB24 3UD, UK. [2]Department of Earth Sciences, Open University, Milton Keynes MK7 6AA, UK.

*To whom correspondence should be addressed. E-mail: spherules@abdn.ac.uk

events permits a direct tie-in of the impact to the stratigraphic record and an assessment of its timing and related environmental and biotic consequences.

Our deposit contains spherules and shocked quartz, which are diagnostic evidence of an impact ejecta layer. The ejecta deposit is located within a late Triassic continental red mudstone/sandstone succession in a temporary exposure near Bristol in southwestern Britain. The stratigraphic succession is a marginal facies of the Mercia Mudstone Group (Norian) positioned below the horizon of the widely recognized late Triassic Rhaetian marine transgression (Late Norian, Penarth Group) (Fig. 1 and fig. S1). The position of this layer in red continental sediments below the base of the Penarth Group places it within the upper part of the local Triassic succession but well below the Triassic/Jurassic boundary.

The ejecta layer was found 1 m from the base of a 9-m-thick deposit of Mercia Mudstone that unconformably overlies the regional Lower Carboniferous (Dinantian) limestone basement. The ejecta layer ranges in thickness from 0 to 150 mm (average of 25 mm from eight points that were sampled within a 200-m-wide region) and shows evidence of turbulent reworking in water such as grading, convolution, rippling, and mixing with local mud and lithoclasts. The layer contains up to 50% (by rock volume) emerald green spherules preserved within a clear calcite and/or pink potassium feldspar matrix. Spherules are mostly in the submillimeter-size range. They are usually round, but other shapes are found, including teardrops, dumbbells, fractured spheres, and shards (Fig. 2). Spherules are composed of disordered illitic clay (Fig. 3), and many are hollow, or were so before the arrival of diagenetic minerals. Spherule exteriors are generally smooth, whereas interiors have a botryoidal texture (Fig. 3). Spherules commonly enclose one or more smaller spheres (Fig. 2), in which the smooth surface is the inside and the botryoidal one the outside, reversing the order in the host spherule. Concentric zonation within spherule walls is commonly marked by clusters of micrometer-sized titanium oxide crystals.

Spherules of this type are generally considered to be pseudomorphs after glass beads (microtektites) that solidified from molten and vaporized material generated during shock melting and explosive vaporization of terrestrial or extraterrestrial materials (*5–7*). Spherule shapes result from surface tension and aerodynamic flight of molten glass, followed by quenching in either air or water (*8–10*). Our spherules are similar in shape and texture to those found in the end-Cretaceous (Cretaceous-Tertiary event, commonly called K/T) impact deposit, particularly Type 1 spherules in the K/T (*10*), which have similar simple, distorted, conjoined, compound and fractured morphologies (*8–10*). K/T spherules at some sites are also typically hollow, concentrically zoned, and radially textured, having been altered from glass to clay (*8*, *9*, *11*). Alteration starts with hydration of the glass, followed by conversion into stable clay minerals (*9*). Botryoidal inner-wall textures (Fig. 3) mark the limit of crystallization advancement through hydrated glass, and the hollow interiors of spherules result from the loss of the remaining glass during later diagenesis (*9*). Compound sphere-within-sphere forms, with their associated textural reversal, represent vesicular glass (*9*).

Quartz grains are abundant in the late Triassic ejecta deposit, but concentration varies throughout. Some of this quartz was probably entrained from local sediment during reworking, but we have etched representative quartz residues in hydrofluoric acid to look for shocked quartz, which is diagnostic of high-energy impact events (*12*). Separated grains were mostly angular, in the 50- to 300-μm range, and although about 50% showed no response, the remainder were strongly etched, displaying abundant planar

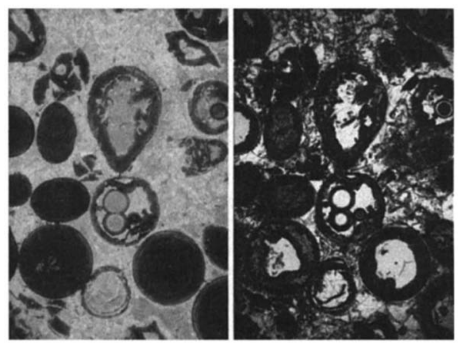

Fig. 2. Cathodoluminescence (**left**) and transmitted light (**right**) images of Triassic spherules and shards in a calcite matrix. Spherical, oblate, teardrop, and sphere-within-sphere forms, as well as shards, are apparent. Clay and empty space are nonluminescent; calcite is bright. (Polished standard optical thin section, width of field ~2 mm.)

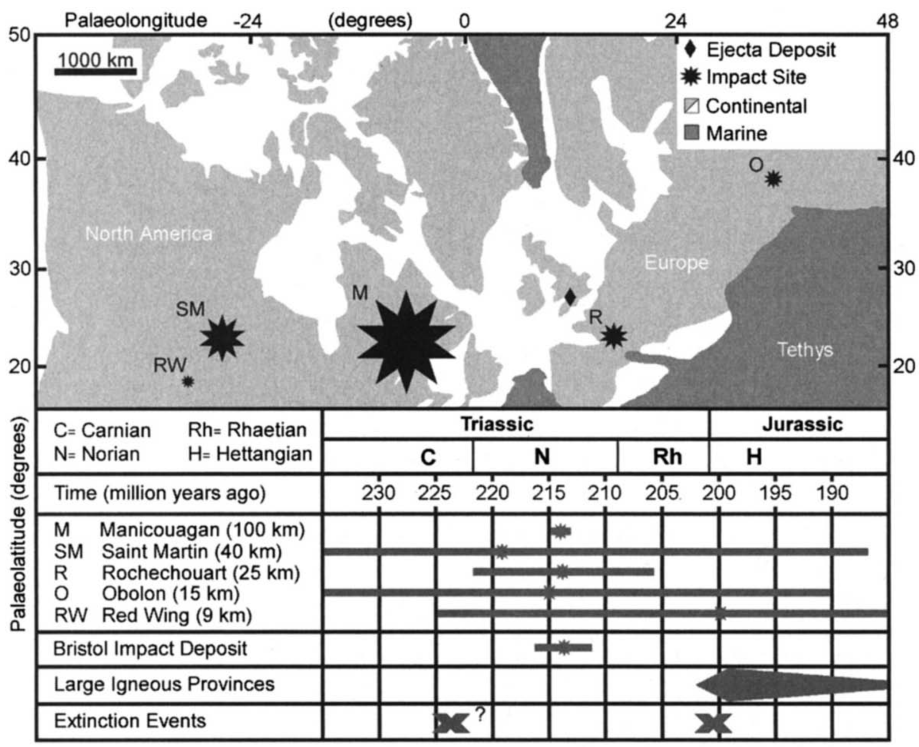

Fig. 1. Late Triassic impact sites in relation to the southwest Britain impact deposit placed on a North American/Eurasian plate reconstruction of ~214 Ma [after Spray *et al.* (*1*)]. Impact symbols are scaled according to relative (not absolute) size of impact crater. Full extent of some error values is not shown. Large Igneous Provinces data are from (*16*). Carnian Extinction is derived from Benton (*3*).

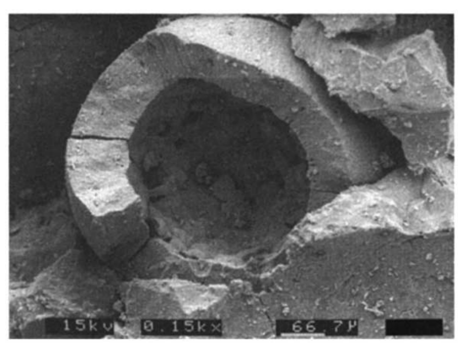

Fig. 3. A Triassic clay spherule set in a calcite matrix. The outer wall of a second spherule occupies top left of the image. (Scanning electron microscope secondary electron image; the spherule is 0.5 mm.)

layers arranged in parallel sets with multiple orientations. These may be impact-generated planar deformation features (PDFs) (*13*), each marked by a layer of quartz glass that has been preferentially removed during etching (Fig. 4). U-stage measurements of these planar features, conducted by established optical procedures (*14*), provided rational Miller indices and confirmed their identity as shock effects. Orientation data included high counts of {10$\bar{1}$2} (~26%) and {10$\bar{1}$3} (~42%) (Fig. 5), confirming impact-generated shock pressures (*13*).

Ar-Ar dates were obtained from inter- and intragranular authigenic K-feldspar, which was separated from the deposit and washed in a dilute acid to remove carbonate. Laser step heating has yielded old ages in the first few steps of ^{39}Ar release and slightly noisy plateaus, although most of the Ar release occurs at relatively low temperatures (table S1; fig. S2). We obtained a low-precision plateau age of 214 ± 2.5 million years ago (Ma) (2σ errors). Because the K-feldspar (5 to 10 μm) is authigenic, it postdates the age of spherule deposition, but dissolution of the glass of spherule cores may have provided the ions necessary to cause early K-feldspar diagenesis, a common feature of continental red-bed deposits (*15*).

Our Ar-Ar age is consistent with a Norian age of the layer on the basis of the local stratigraphy, indicating that the impact event occurred before the end of the Triassic, which has recently been placed at about 201 Ma (*16*). This Ar-Ar age is within the dating errors of the two best-constrained of the late Triassic craters (Fig. 1), which are the Manicouagan crater in northeastern Canada (214 ± 1 Ma, U-Pb) (*17*) and the Rochechouart crater in central France (214 ± 8 Ma, Ar-Ar) (*18*). We estimated the possible ejecta layer thickness at various distances from these potential source craters to determine which crater may have produced the deposit. Several variables influence the thickness and distribution of an ejecta blanket, including impact dynamics (size, velocity, impact angle, and Earth's rotation) and impact site characteristics (crystalline or sedimentary target), but basic crater size and distance models (*19–21*) suggest a difference in the ejecta layer thickness in southwestern Britain from the two sources. A deposit from Manicouagan (100-km-diameter crater and about 2000 km away from the layer on the basis of a late Triassic plate reconstruction) (Fig. 1) would be about 6.6 to 15.5 mm thick, whereas one from Rochechouart (25-km-diameter crater and 650 km away) would be 1.1 to 1.6 mm thick (table S2). Local thickness variation and mixing of the actual deposit prevent accurate averaging, but our figure of ~25 mm includes at least 10 mm of impact-derived spherules and dust. From first approximation thickness modeling, therefore, Manicouagan may be a source for the layer, but we cannot rule out the possibility that the ejecta may be from the Rochechouart crater or from both craters as part of a multiple-impact event (*1*). The deposit could be a sedimentary record of an impact event of global significance at this time and, if so, there is no corresponding biotic response in the fossil record (Fig. 1).

Given the Ar-Ar date of ~214 Ma, we can predict the position of the deposit in British and North American successions. On the basis of magnetostratigraphic work linked to cyclostratigraphy (*22*, *23*), the position of the layer can be correlated with paleomagnetic chron E14 (fig. S1). This lies within the lowest part of the Passaic Formation in the Newark Basin and within the Twyning Mudstone Formation in North Somerset, England. No ejecta deposits have hitherto been reported from either of these successions. The only other ejecta deposits associated with an impact event in the late Triassic are the discovery of shocked quartz at the Triassic/Jurassic boundary in Italy (*24*) and a small iridium anomaly at the Triassic/Jurassic boundary in the Newark Basin succession (*4*). Our ejecta layer is located in a stratigraphic succession below the boundary and will provide a valuable time horizon in sedimentary successions, but only if it is widespread. In the generally arid continental environments of the Triassic, the preservation potential of microtektites may have been reduced by the lack of standing water, considered essential for the hydration and palagonitization process (*9*). Microtektites may have remained as glass, which can be removed during diagenesis (*9*). More work is needed to confirm the age of our deposit and to look for related deposits elsewhere that might be part of a global event.

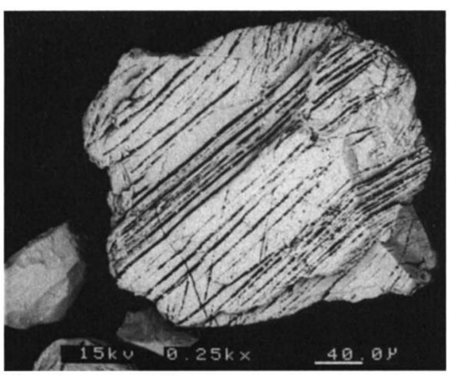

Fig. 4. A quartz grain from the Triassic impact deposit displaying two differently oriented parallel sets (approximately north-south and northeast-southwest) of shock lamellae (PDF). There are up to three additional subsidiary sets in other orientations. Acid etching has removed quartz glass, and some lamellae reveal quartz annealment (syntaxial regrowth) features. (Scanning electron microscope secondary electron image.)

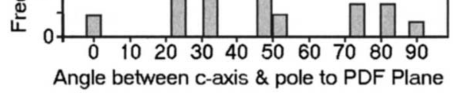

Fig. 5. Histogram of frequency percentage of angles between *c* axis and poles to the planes of PDF angles for 33 grains in part of one thin section. Data were plotted using ± 5° error circles with rotation to best fit (*14*). Five grains show 1 PDF direction, 17 show 2 PDF directions, 8 show 3 PDF directions, 2 show 4 PDF directions, and 1 shows 5 PDF directions. In some cases additional PDF directions were detected but could not be measured. The grains reveal a mixed population of impact stresses, but 10 showed only {10$\bar{1}$2} or {10$\bar{1}$2} + {10$\bar{1}$3}, which is the highest shock state before complete phase transformation.

References and Notes

1. J. G. Spray, S. P. Kelley, D. P. Rowley, *Nature* **392**, 6672 (1998).
2. C. Koeberl, V. L. Sharpton, *Lunar Planet. Inst.* Contribution **1083** (2001).
3. M. Benton, in *In the Shadow of the Dinosaurs*, N. C. Fraser, H. D. Sues, Eds. (Cambridge Univ. Press, Cambridge, UK, 1994), pp. 366–397.
4. P. E. Olsen *et al.*, *Science* **296**, 1305 (2002).
5. C. Koeberl, in *Large Meteorite Impacts and Planetary Evolution: Special Paper 293*, B. O Dressler, R. A. F. Grieve, V. L. Sharpton, Eds. (Geological Society of America, Boulder, CO, 1994), pp. 133–151.
6. B. P. Glass, *Tectonophysics* **171**, 393 (1990).
7. W. Alvarez, in *The Cretaceous-Tertiary Event and Other Catastrophes in Earth History: Special Paper 307*, G. Ryder, D. Fastovsky, S. Gartner, Eds. (Geological Society of America, Boulder, CO, 1996), pp. 141–150.
8. B. P. Glass, D. W. Muenow, B. F. Bohor, G. P. Meeker, *Meteoritics* **32**, 333 (1997).
9. B. F. Bohor, B. P. Glass, *Meteoritics* **30**, 182 (1995).
10. B. F. Bohor, W. J. Betterton, *Lunar Planet. Sci. (abstract)* **XXIII**, 135 (1990).
11. G. A. Izett, *J. Geophys. Res.* **96**, 20879 (1991).
12. J. A. Bostwick, F. A. Kyte, in *The Cretaceous-Tertiary Event and Other Catastrophes in Earth History: Special Paper 307*, G. Ryder, D. Fastovsky, S. Gartner, Eds. (Geological Society of America, Boulder, CO, 1996), pp. 403–415.
13. R. A. F. Grieve, F. Langenhorst, D. Stoffler, *Meteoritics* **31**, 6 (1996).
14. W. Engelhardt, W. Bertsch, *Contrib. Mineral. Petrol.* **20**, 203 (1969).
15. T. R. Walker, B. Waugh, A. J. Crone, *Geol. Soc. Am. Bull.* **89**, 353 (1978).
16. J. Pálfy *et al.*, *Geology* **28**, 39 (2000).
17. J. P. Hodych, G. R. Dunning, *Geology* **20**, 51 (1992).
18. S. P. Kelley, J. G. Spray, *Meteoritics* **32**, 171 (1997).
19. R. D. Lorenz, *Icarus* **144**, 353 (2000).

20. T. R. McGetchin, M. Settle, J. W. Head, *Earth Planet. Sci. Lett.* **20**, 226 (1973).
21. D. Stoffler, D. E Gault, J. Wedekind, G. Polkowski, *J. Geophys. Res.* **80**, 29 (1975).
22. P. E. Olsen, D. V. Kent, R. Raeside, "International workshop for a climatic, biotic, and tectonic, pole-to-pole coring transect of Triassic-Jurassic Pangea" (International Continental Scientific Drilling Program, Potsdam, 1999), vol. 1; www.ldeo.columbia.edu/~polsen/nbcp/icdp.abst.html.
23. M. W. Hounslow, G. Warrington, P. E. Posen, poster presented at the International Geological Correlation Programme (IGCP) 458 Southwest England Field Workshop: Jurassic/Triassic Boundary Meeting, Taunton, UK, October 2001; http://geography.lancs.ac.uk/cemp/publications/01houns-sta_abs.htm.
24. D. M. Bice, C. R. Newton, S. McCauley, P. W. Reiners, C. A. McRoberts, *Science* **225**, 443 (1992).
25. We thank J. Whitehead for his guidance on measuring planar deformation features in quartz using a u-stage.

Supporting Online Material
www.sciencemag.org/cgi/content/full/1076249/DC1
Figs. S1 and S2
Tables S1 and S2
References

17 July 2002; accepted 5 November 2002
Published online 14 November 2002;
10.1126/science.1076249
Include this information when citing this paper.

Heart Regeneration in Zebrafish

Kenneth D. Poss,* Lindsay G. Wilson, Mark T. Keating*

Cardiac injury in mammals and amphibians typically leads to scarring, with minimal regeneration of heart muscle. Here, we demonstrate histologically that zebrafish fully regenerate hearts within 2 months of 20% ventricular resection. Regeneration occurs through robust proliferation of cardiomyocytes localized at the leading epicardial edge of the new myocardium. The hearts of zebrafish with mutations in the Mps1 mitotic checkpoint kinase, a critical cell cycle regulator, failed to regenerate and formed scars. Thus, injury-induced cardiomyocyte proliferation in zebrafish can overcome scar formation, allowing cardiac muscle regeneration. These findings indicate that zebrafish will be useful for genetically dissecting the molecular mechanisms of cardiac regeneration.

Injured human hearts do not regenerate. Instead, damaged myocardium is replaced by fibrotic scar tissue. Cardiomyocytes, the major structural cells of the heart, may undergo hypertrophy in the wound area to increase muscular mass. Although recent findings suggest that cardiomyocytes within the diseased human heart can proliferate (*1*), most evidence to date indicates that myocyte proliferation is not a significant component of the mammalian response to cardiac injury (*2*).

Teleost fish, including zebrafish, can regenerate spinal cord, retina, and fins (*3*, *4*). To determine whether zebrafish can also regenerate heart muscle, we surgically removed ~20% of the ventricular myocardium from 1- to 2-year-old adults (Fig. 1, A and B) and

Department of Cell Biology, Department of Cardiology, Howard Hughes Medical Institute, Harvard Medical School, Children's Hospital, 320 Longwood Avenue, Boston, MA 02115, USA.

*To whom correspondence should be addressed. E-mail: kposs@enders.tch.harvard.edu(K.D.P.); mkeating@enders.tch.harvard.edu (M.T.K.)

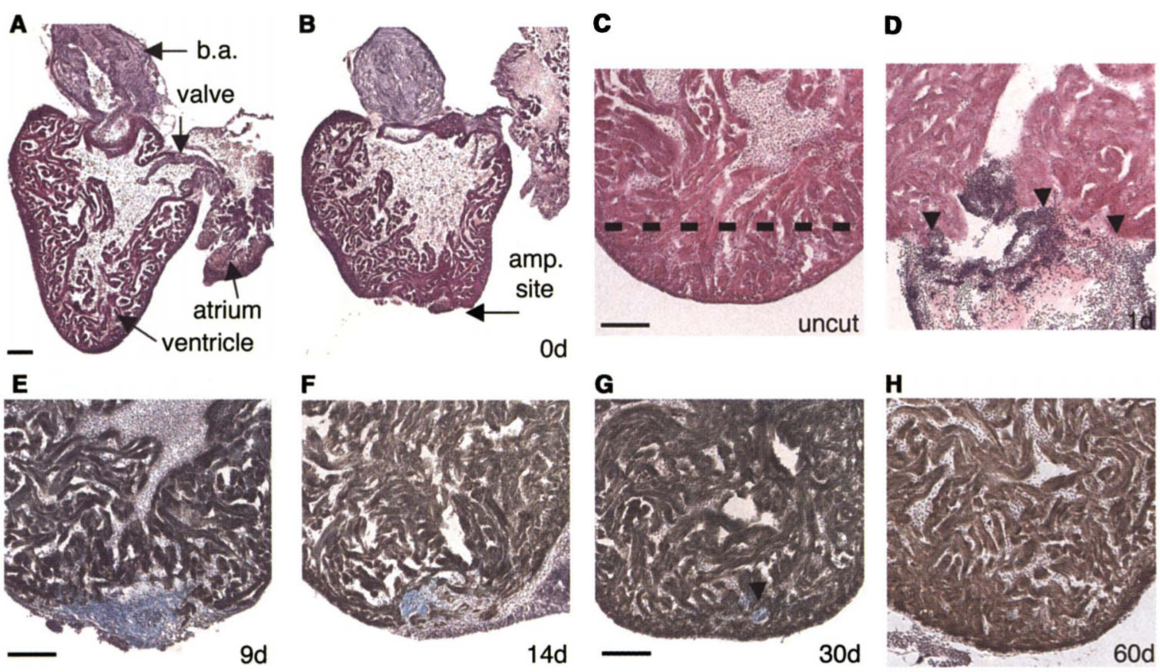

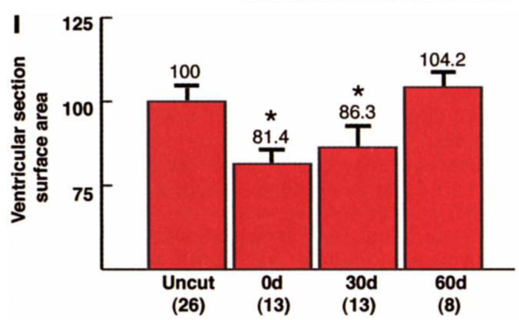

Fig. 1. Regeneration of ventricular myocardium in the resected zebrafish heart. Hematoxylin and eosin stain of the intact zebrafish heart before (**A**) and after about 20% ventricular resection (**B**) (*5*). b.a., bulbous arteriosus. (**C**) An intact ventricular apex at higher magnification, indicating the approximate amputation plane (dashed line). All images in this and subsequent figures display longitudinal ventricular sections of the amputation plane. (**D**) 1 dpa. The large clot is filled with nucleated erythrocytes (arrowheads). (**E**) 9 dpa. The heart section is stained for the presence of myosin heavy chain to identify cardiac muscle (brown) and with aniline blue to identify fibrin (blue) (*5*). The apex is sealed with a large amount of mature fibrin. (**F**) 14 dpa. The fibrin has diminished, and the heart muscle has reconstituted. (**G**) 30 dpa. A new cardiac wall has been created, and only a small amount of internal fibrin remains (arrowhead). (**H**) 60 dpa. This ventricle shows no sign of injury. (**I**) Quantification of healing at 0, 30, and 60 dpa. Values represent the size of the largest ventricular section (mean ± SEM; *$P < 0.05$); parentheses indicate the number of hearts examined (*5*). Scale bars, 100 μm.